Article

Towards an Optimization of Sample Plot Size and Scanner Position Layout for Terrestrial Laser Scanning in Multi-Scan Mode

Tim Ritter *[ID], **Christoph Gollob**[ID] and **Arne Nothdurft**[ID]

Department of Forest- and Soil Sciences, Institute of Forest Growth, University of Natural Resources and Life Sciences, Vienna (BOKU), 1180 Vienna, Austria; christoph.gollob@boku.ac.at (C.G.); arne.nothdurft@boku.ac.at (A.N.)
* Correspondence: tim.ritter@boku.ac.at; Tel.: +43-1-47654-91414

check for updates

Abstract: A novel approach is presented to model the tree detection probability of terrestrial laser scanning (TLS) in forest inventory applications using a multi-scan mode. The traditional distance sampling framework is further extended to account for multiple scan positions at a single sample plot and to allow for an imperfect detection probability at distance $r = 0$. The novel methodology is tested with real world data, as well as in simulations. It is shown that the underlying detection model can be parameterized using only data from single scans. Hereby, it is possible to predict the detection probability also for different sample plot sizes and scanner position layouts in a multi-scan setting. Simulations showed that a minor discretization bias can occur if the sample size is small. The methodology enables a generalized optimization of the scanning layout in a multi-scan setting with respect to the detection probability and the sample plot area. This will increase the efficiency of multi-scan TLS-based forest inventories in the future.

Keywords: TLS; LiDAR; forest inventory; scanning layout; scan positions

1. Introduction

Forest inventories provide relevant information on the status and changes of forest landscapes. Traditionally, forest inventories were designed to provide precise information on the timber growing stock. However, over the last decades, catalogues of key attributes surveyed in forest inventories have been broadened [1] in the context of redefined goals of a sustainable forest management [2]. A modern multi-purpose forest inventory also considers aspects of biodiversity and carbon sequestration [3,4]. Until now, tree attributes and positions are manually measured in forest inventories, using simple mechanical or optical instruments, such as calipers, hypsometers, compasses, and measuring tapes [1,5,6]. Thus, measurements of tree attributes with the traditional instruments are time-consuming, cost-intensive, and prone to manifold measurement errors; nevertheless, they are still regarded as the gold standard to which new measuring techniques are compared [7–9]. Sampling schemes of forest inventories have been optimized for efficiency and precision [10,11] and can further be adopted in case new sensor techniques replace the traditional measuring equipment in the future.

Terrestrial laser scanning (TLS) has been successfully evaluated in the context of manifold forestry applications, and the automatic detection of trees and the measurement of further attributes in the TLS point clouds have been comprehensively studied using both settings: the single-scan mode [7,8,12–21] and the multi-scan mode [8,14,22–38]. TLS enables a fast and automatic registration of the forest structure [39], especially in the single-scan mode, where only one scan is performed, usually obtained from the sample plot center. However, a relevant proportion of trees cannot be detected

with single-scan TLS. This is because the laser beams are often obstructed by other trees, understory vegetation, or rocks. The problem becomes more pronounced with increasing the distance between the scanner and the tree of interest, simply because, with increasing the distance, the probability of having an obstacle between the scanner and the target increases. Some approaches have been developed to solve the nondetection problem of single-scan TLS. Proper correction methods were either based on geometrical considerations [12,40,41] or on the modeling of the distance-dependent detection probability [21,42]. Since these correction methods require extra computations and suitable model assumptions, the single-scan approach is not often used in practice, and the multi-scan approach is generally preferred, instead.

In the multi-scan mode, the scanner is placed at different locations within the sample plot boundaries or at extra outer positions in order to derive a complete 3D scan of the vegetation and to avoid disturbances by obstruction effects. However, the extra work of the multi-scan mode is associated with higher labor costs and requires data post-processing for the co-registration of the multiple scans. According to Gollob et al. [43], three different types of scanner location configurations can be distinguished, by which the scanner was either located (i) at the boundaries of the sample plot [31,32,34–36,44], (ii) at outer positions beyond the sample plot area [28,29,36,37], or (iii) at the plot center plus at several extra positions within the surrounding area [7,14,22–27,36,38].

Despite its high labor costs, the multi-scan mode was used in a vast number of studies. However, only little is known so far on the efficiency of different scanner position layouts and of the sample plot sizes and shapes when TLS is used in the context of forest inventories. Thus far, the only few existing studies were either simulations [36,38] or real-world experiments [43,45].

Abegg et al. [36] performed a simulation study on the influence of scanner locations and tree stem positions on the occultation of tree stems. Van der Zande et al. [38] simulated the shadowing of the forest canopy structure associated with three different scanner position combinations, each of which were established in three different stand types. Whereas the latter both studies only examined the occultation effects that were produced by other trees, the influence of alternative obstacles, like understory vegetation, rocks, or terrain, was not considered. Moreover, a validation of the simulation results with a real-world scenario was not conducted.

Trochta et al. [45] studied the effect of a sample size reduction on the stem-detection rate in a large area stem-mapping trial when the 40 m × 40 m sampling grid was continuously thinned. Gollob et al. [43] compared eight different multi-scan and single-scan settings in terms of precision and sampling effort on 23 forest inventory sample plots. Thus far, no existing study validated the simulations of the influence of scanner locations on the occultation of tree stems with real-world data.

The major goal of our study was to examine the influence of the sample plot area and the scanner positioning on the detection probability in a multi-scan setting.

We hypothesized that the distance sampling framework [46–49], which has been successfully used for the modeling of the detection probability under the single-scan mode [21,42], can be extended to a broader applicability that also includes the multi-scan case. We further hypothesized that this extended modeling framework can be used to optimize the sample plot area and the scanner positioning to maximize the detection probability in a multi-scan setting.

We show that the detection rate with different scanner position layouts could be generally predicted for different sample plot sizes in order to find an optimal design for a TLS-based forest inventory. The single-scan data from Gollob et al. [43] was recycled for model parameterization, and its validation was performed by means of the multi-scan data from the same study. The model bias was additionally assessed via simulations. The novel approach enables to predict the detection probability for different sample plot sizes and scanner position layouts under multi-scan TLS using prior information from single scans and reference data. Hence, our methodology can be used to optimize the design of TLS-based surveys in forest landscapes.

2. Materials and Methods

2.1. Data

Our methodology was developed by means of existing data, which was formerly collected for the study in Gollob et al. [43]. The same applied to the stem-detection algorithm, which was also adopted from Gollob et al. [43]. Hence, only a brief summary of the dataset and the data-processing routines is presented, and it is referred to Gollob et al. [43] for further details.

The study site was located in the forest district of Ofenbach, in the Lower-Austrian pre-Alps, near the village of Forchtenstein. In total, data from 23 circular sample plots each with a 20 m radius was used. The laser scanning was conducted in February–March 2018 using a FARO Focus3D X330 terrestrial laser scanner (Faro Technologies Inc., Lake Mary, FL, USA). Nine artificial reference targets (Styrofoam balls on monopods) were systematically arranged on the plots; one target was placed directly at the plot center, and four targets were placed at a distance of 5 m from the plot center, so that they formed the corners of a square. The remaining four targets were placed at a distance of 10 m from the plot center, so that they formed another square that was rotated 45° relatively to the first square.

At each of the sample plots, a set of nine scan variants was tested that differed in the positioning of the scanner, as well as in the number of scans per plot. The most intensive scan variant (full scan) was comprised of seven scanner positions. Hereof, six positions were arranged in a regular hexagon with a constant edge length of 15 m and centered at the sample plot center, and an additional scan was conducted from the sample plot center. As another extreme, a single-scan variant was accomplished in which the scanner was placed only at the sample plot center. The other scan variants constituted as subsets of the full scan, comprising a hexagon without a central scan and other geometrical arrangements (triangle, rectangle, and diagonal) and either including or excluding an additional central scan.

Co-registration of the raw scan data was separately performed for each scan variant and by means of the reference targets using the FARO SCENE 6.2 software [50]. A noise-filtering, ground point classification and point cloud normalization to remove the height offset was performed using the LAStools software package [51]. For the automated tree detection [9,43], we used a density-based clustering algorithm [52] that was implemented in the R language and environment [53]. More precisely, the stem detection algorithm [9,43] was based on a density-based clustering applied in two subsequent phases. In the first clustering phase, the 3D point cloud of normalized Z values was stratified into vertical layers, and a density-based clustering was separately applied to a subsample of the points selected from each layer. Prior to the second phase, the cluster centroids from the first phase were projected onto a horizontal plane, and a density-based clustering was subsequently applied to this set of points in 2D. The resulting phase 2 cluster centroids were then used as preliminary tree position estimates. The final tree position estimates were achieved through a further distance-based filtering and heuristic decision rules to decide whether a detected cluster actually is a tree based on estimated diameters in different heights. Reference data was also available from manual measurements of the positions and diameters at breast height (dbh) of all trees having a dbh ≥ 5 cm [43].

2.2. Modeling the Detection Probability of TLS in Single-Scan Mode

2.2.1. Classic Distance Sampling Approach

The basic idea of distance sampling [47,48] is that the detectability of objects typically decreases with increasing distance r between the observer (i.e., the laser scanner in our application) and the object of interest (i.e., a tree). By fitting a distance-dependent detection function $g(r)$ to the normalized

density of observed objects at different distances ($0 \leq r \leq \omega$), the mean detection probability within a circular sample plot of area a and radius ω can be estimated by

$$\hat{P}_a = \frac{2}{\omega^2} \int_0^{\omega} r \times g(r)dr \tag{1}$$

For normalization, the density of detected objects in every distance interval is divided by the estimated density of all objects [47].

The fundamental assumptions underlying this approach are (i) that trees located directly at the plot center ($r = 0$) are detected with certainty ($g(0) = 1$) and (ii) that the detection probability decreases monotonously with increasing distance from the plot center. The detection function g is usually represented by a parametric function and can be fitted using maximum-likelihood techniques [47,48]. Although it is also possible to use nonparametric representations of g [54], parametric models are generally preferred, instead. This is because the parametric functions provide sufficient flexibility, and their inference is straightforward.

Thus far, distance sampling has been used with single-scan TLS data by Ducey and Astrup [21] and by Astrup et al. [42] using half-normal [21] and hazard-rate [42] detection functions. In our study, trials were made with three parametric candidate functions: the half-normal, the uniform, and the hazard-rate function. Hereof, the hazard-rate function

$$g_{hr}(r) = 1 - e^{-\left(\frac{r}{\sigma}\right)^{-b}} \tag{2}$$

showed the best performance in terms of the AIC (Akaike's Information Criterion [55]) (Table 1).

Table 1. AIC (Akaike's Information Criterion)-based comparison of the candidate detection functions.

Type of Detection Function	Formula	AIC	Δ AIC
hazard-rate	$g_{hr}(r) = 1 - e^{-\left(\frac{r}{\sigma}\right)^{-b}}$	5634.72	0.00
half-normal	$g_{hn}(r) = e^{\left(\frac{-r^2}{2\sigma^2}\right)}$	5640.31	5.59
uniform	$g_{unif}(r) = 1/\omega$	5637.58	2.86

r is the distance between the scanner and an object of interest; ω is the overall detection truncation distance; a, b, and σ are function-specific parameters; and Δ AIC is the AIC difference between the candidate model and the chosen model.

The hazard function had two parameters: a shape coefficient σ and scale coefficient b [47]. Model fitting was accomplished in R [53] using the Distance package [56]. The hazard-rate detection function should generally meet the fundamental assumption of distance sampling of a perfect detectability at $r = 0$, thus $g_{hr}(0) = 1$ (for all σ, $b > 0$) [47].

2.2.2. Correction for Imperfect Detectability at $r = 0$

Our preliminary results showed that the assumption of a perfect detectability at $r = 0$ ($g(0) = 1$) was not met. Hence, an uncritical adoption of Equation (2) without checking the validity of the assumptions would have resulted in a biased estimate of P_a. Thus, an additional factor c was introduced to Equation (2), yielding

$$g_{ehr}(r) = c \times \left(1 - e^{-\left(\frac{r}{\sigma}\right)^{-b}}\right) \tag{3}$$

where c ($1 \geq c > 0$) represents the initial detection probability at $r = 0$.

However, the representation in Equation (3) cannot be fitted to the normalized density of the observed objects at different distances, as the normalization procedure depends on the assumption that $g(0) = 1$. As a solution, the observed distances of the detected trees were discretized into

1 m wide classes, and $g_{ehr}(r)$ was fitted to the average detection probabilities within these classes. The average detection probabilities were calculated by means of manual reference data that were additionally required. Parameter estimation was performed using an adaptive nonlinear least-squares algorithm [57], which was implemented in the R function "nls()" [53].

The parameter estimates were then used in the modified hazard rate function (Equation (3)) to predict the probability P_j that a tree located at position j is actually detected given the location-scanner distance r_j. More precisely, P_j was calculated for all the raster cell centroids of a two-dimensional raster with cell size 1 cm × 1 cm and assigned to the corresponding cell values.

Finally, the arithmetic mean of all raster cell values within a sample plot of corresponding radius ω was used as the estimate of P_a. Due to the fact that large trees generally had a higher detection probability than small trees [42], the 3894 trees on the 20 m radius sample plots were stratified into 2829 smaller trees (5 cm ≤ dbh < 20 cm) and 1065 larger trees (dbh ≥ 20 cm), and the modeling of the detection function, as well as the prediction of the mean detection probability, was independently conducted for both strata. A higher number of strata was desirable; however, this would have resulted in a lower within-strata sample size that would have become problematic when modeling the detection probability for the smaller sample plot radii. For a sample plot radius of $\omega = 5$ m, as an example, the sample size was reduced to 261 trees, 73 of which were large trees and 188 of which were small trees, and for $\omega = 2$ m, the sample size was reduced to 51 trees (15 large trees and 36 small trees).

2.3. Modeling the Detection Probability of TLS in Multi-Scan Mode

In the previous sections, the dependence of the detection probability on the distance to the scanner was outlined for single-scan TLS and the detection probability at distance r was modeled using the detection function $g(r)$. In the following paragraphs, a generalization of the methodology from the single-scan mode to the multi-scan mode is established. In general, and with regard to the multi-scan mode with I scanner positions, a set of I point-to-scanner distances can be measured for each location within the sample plot area.

First, let us assume that the probability of detecting an arbitrary tree j located in a distance of r_{ij} from the scanner position i is independent from the probability to detect the same tree from any other scanner position: $i' \neq i$ for $i', i \in \{1, \ldots, I\}$ and that this probability can be estimated by $g(r_{ij})$. Thus, the complementary probability of missing an arbitrary tree j located in a distance of r_{ij} from the scanner position can be estimated as $1 - g(r_{ij})$.

From this follows that the probability to miss this tree from all I scanner positions is

$$\prod_{i=1}^{I}\left(1 - g\left(r_{ij}\right)\right) \tag{4}$$

and the corresponding probability to detect a tree located on point j becomes

$$P_j = 1 - \prod_{i=1}^{I}\left(1 - g\left(r_{ij}\right)\right) \tag{5}$$

Depending on a possible violation of the assumptions underlying the classic distance sampling approach, $g(r_{ij})$ can be estimated either by using the classic distance sampling approach with different possible detection function types or by using its above-described modification, which accounts for an imperfect detectability at $r_{ij} = 0$. In case the extended hazard function is used, a replacement of Equation (3) into Equation (5) yields.

$$P_j = 1 - \prod_{i=1}^{I}\left(1 - g_{ehr}\left(r_{ij}\right)\right) = 1 - \prod_{i=1}^{I}\left(1 - c \times \left(1 - e^{-\left(\frac{r_{ij}}{\sigma}\right)^{-b}}\right)\right) \tag{6}$$

In the following sections, we examined whether the parameters c, b, and σ in Equation (6) can be estimated by using only the single-scan TLS data (Section 2.2.2). That is, only the data obtained from the central scan position was used for the model fitting of the detection function, and the data from the

other positions were simply neglected. Henceforth, Equation (6) was used to predict the detection probability for all cells of a two-dimensional raster with a cell size of $1\,\text{cm} \times 1\,\text{cm}$ and dependent on the distances of the raster cell centroids to the I different scanner locations.

Analogous to the procedure in Section 2.2, the mean detection probability P_a per sample plot was estimated via the average of all raster cell estimates P_j within the plot:

$$\hat{P}_a = \frac{1}{J} \sum_{j=1}^{J} \left(1 - \prod_{i=1}^{I} \left(1 - c \times \left(1 - e^{-\left(\frac{r_{ij}}{\sigma}\right)^{-b}} \right) \right) \right) \tag{7}$$

where J is the total number of raster cells per sample plot.

The entire methodology was tested for different sample plot radii ω and different scan variants and separately applied to both strata (smaller trees and larger trees). These model-based estimates of the detection probability were compared with the global P_a^* estimates, which were empirically derived by means of the reference data of the complete tree list.

2.4. Model Evaluation

2.4.1. Case Study Data

Trees from the complete reference data that were detected by the automatic routines applied to the TLS data were coded as a binary variable: 1—detection and 0—non-detection. A global estimate P_a^* of the true detection probability P_a was derived via the average of the binary observations over all sample plots. Both the empirical estimate P_a^* and the model-based estimate $\hat{P}_a$ were computed.

Confidence limits (*CL*) of P_a^* under error rate α were estimated via a normal approximation (Equation (8)):

$$CL = P_a^* \pm z \times \sqrt{\frac{P_a^* \times (1 - P_a^*)}{n}} \tag{8}$$

with z being the $1\text{-}\alpha/2$ quantile of a standard normal distribution and n as the number of observed trees within all sample plots.

To assess the model performance under different sample plot sizes and scanner position layouts, the model-based estimate $\hat{P}_a$ was compared with the empirical estimate P_a^* independently for the different settings and for both tree size strata and across a dense sequence of sample plot radii.

2.4.2. Simulation

In order to assess whether the model could possibly produce a bias even in case all model assumptions are met, a simulation with 200 runs was additionally performed, separately for both tree size strata, using the language and environment R [53]. Thus, tree positions on twenty-five sample plots were simulated within a program loop by assuming that their spatial distributions followed a Poisson point process with variable intensity λ for every sample plot. λ was randomly chosen from a truncated uniform distribution, having the same range as the observed real-world data of the corresponding stratum. For each tree on each sample plot, the distance to every scanner position was calculated, and the corresponding detection probability was independently simulated for every scanner position using the value of the distance-dependent detection function in Equation (6) with the parameters that were obtained by fitting the function to the real-world data of the corresponding stratum. A tree was marked as a detected individual if it was detected from at least one scanner position, i.e., if its simulated detection probability was larger than or equal to a uniformly distributed random number from a closed [0,1] interval. Hence, P_a was a priori known for each of the simulation runs.

The simulated scanner-to-tree distances were binned into 1 m wide classes, and models for the detection functions were separately fitted to the data of both tree size strata and from each of the 200 simulation runs. In summary, this procedure resulted in a set of 200 $\hat{P}_a$ estimates per stratum.

Finally, the expectation of the model-based estimator $(\hat{E}(\hat{P}_a))$ was estimated by the arithmetic mean of these 200 estimates.

The model bias was separately estimated for both strata and for different sample plot radii

$$\text{bias} = \hat{E}(\hat{P}_a) - P_a \tag{9}$$

To examine whether the discretization of the scanner-to-tree distances into 1 m wide classes could have influenced the model bias, 200 extra simulations were performed using 10 cm wide classes and a larger number of 250 sample plots.

3. Results

3.1. Modeling the Detection Probability of TLS in Single-Scan Mode

3.1.1. Classic Distance Sampling Approach

The hazard rate-type detection function achieved a good fit to the normalized density of the observed scanner tree distances (Figure 1a); the parameter estimates were $\sigma = 10.497$ and $b = 3.119$. However, when compared with the empirical detection rates for the 1 m wide annuli, a severe misfit became obvious (Figure 1b). The model would predict a complete detection of trees standing within a range of less than 7 m from the sample plot center. This was because of the a priori assumption of a complete detection at the plot center $g(0) = 1$, in conjunction with the typically strong shoulder of the hazard-rate detection function. Thus, the model predictions did not fit the observed data (Figure 1b), even though the detection function was able to represent the shape of the normalized densities (Figure 1a). Hence, the misfit was not caused by the shape constraints, but it resulted from the improper assumption of $g(0) = 1$.
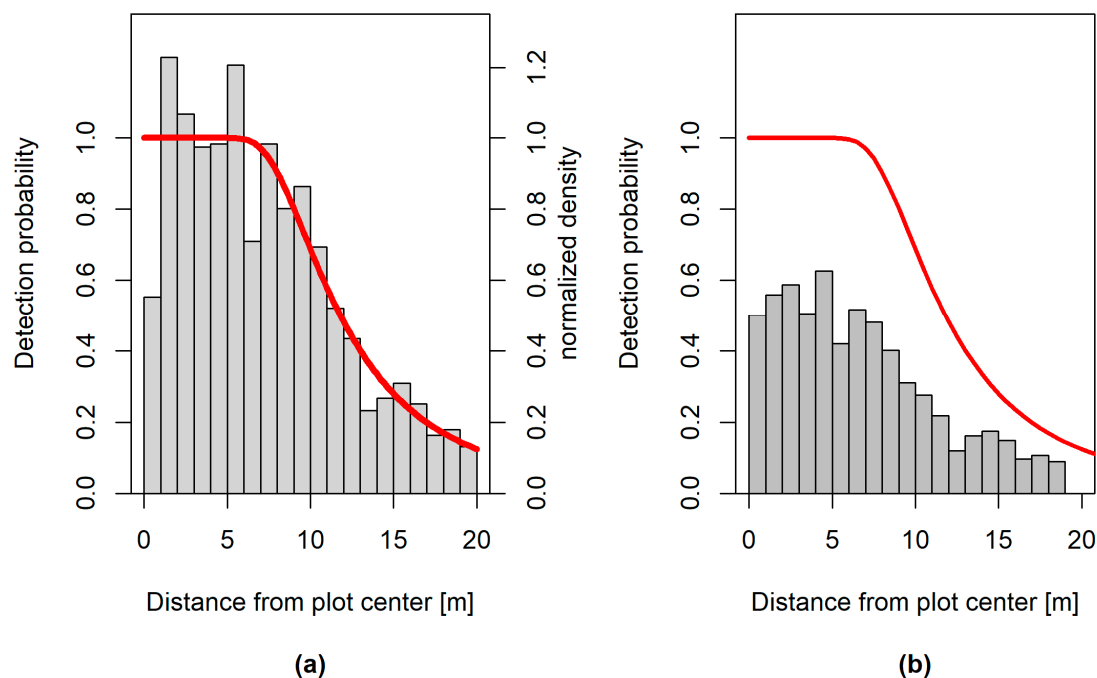

(a)　　　　　　　　　　　　　　　　　　　　**(b)**

Figure 1. Hazard rate-type detection function $g_{hr}(r)$ (red line) for all trees having a diameter at breast height (dbh) ≥ 5 cm. (**a**) $g_{hr}(r)$ fitted to the normalized density of observed distances between the plot center (i.e., scanner position) and detected trees (gray columns); (**b**) $g_{hr}(r)$ compared with the observed detection probabilities at different distances, computed from annuli of 1 m width (gray columns).

By using the classic distance sampling approach under the latter assumptions, the average predicted detection probabilities would produce a severe overestimation, for a broad range of sample plot radii, in comparison with the empirical detection rates (Table 2).

Table 2. Estimated and observed mean detection probabilities for different sample plot radii using classic distance sampling.

Sample Plot Radius ω (m)	Estimated Mean Detection Probability $\hat{P}_a$(%)	Observed MeanDetection Probability P_a(%) (Gollob et al. [43])
5	100.00	63.41
10	91.54	58.57
15	65.21	44.31
20	44.84	34.36

3.1.2. Empirical Results with a Correction for Imperfect Detectability at $r = 0$

To consider the imperfect detectability at $r = 0$, the extended hazard detection function was directly fitted to the un-normalized empirical detection rates on the 1 m annuli. More precisely, the model was separately fitted to both tree size strata; see Figure 2 and parameter estimates in Table 3. Model coefficient c represented the detection probability at $r = 0$. For the stratum of the smaller trees (5 cm $\leq$ dbh < 20 cm), the estimated detection probability at $r = 0$ was 45.29%, and for the stratum of the larger trees (dbh $\geq$ 20 cm), the estimate was 74.26% (Figure 2b).

(a)　　　　　　　　　　　　　　　　(b)
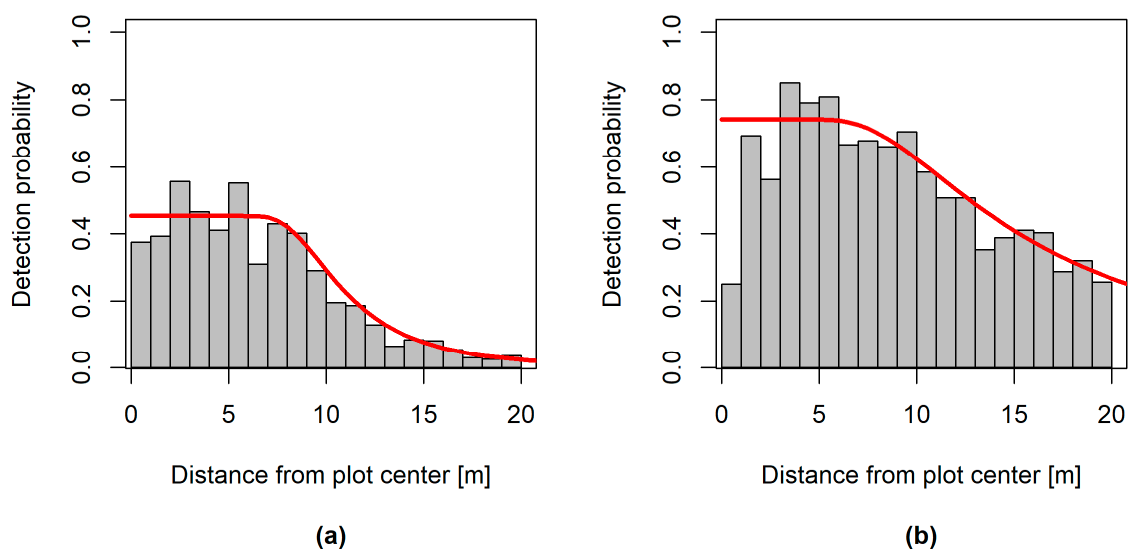
Figure 2. Detection probability $g(r)$ at different distances r from the plot center for both strata. Grey bars represent the observed detection probabilities, and the fitted hazard rate-type models $g_{hr}(r)$ are shown as red curves. (**a**) Small trees (5 cm $\leq$ dbh < 20 cm) and (**b**) large trees (dbh $\geq$ 20 cm).

Table 3. Parameter estimates for the extended hazard rate-type detection function for both strata.

Parameter	Small Trees (5 cm $\leq$ dbh < 20 cm)	Large Trees (dbh $\geq$ 20 cm)
c	0.4528	0.743
σ	10.064	13.446
b	4.263	2.039

These models were subsequently used to predict the detection rates at the grid points of the dense 1 cm × 1 cm raster (Figure 3).
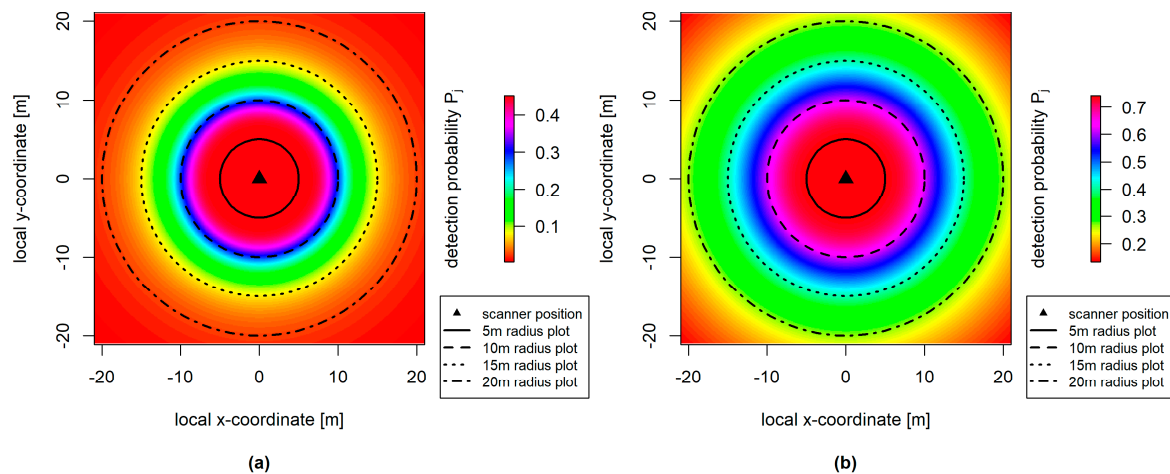
Figure 3. Distance-dependent detection probabilities P_j of single-scan terrestrial laser scanning (TLS) for both strata. Cell size of the raster is 1 cm × 1 cm. (**a**) Small trees (5 cm ≤ dbh < 20 cm) and (**b**) large trees (dbh ≥ 20 cm).

Finally, the global estimate of the mean detection probability P_a was calculated via the average of the predicted detection rate within a sample plot of certain radius ω (Figure 3). In fact, global P_a estimates were computed for a sequence of different ω values ranging from 3 to 20 m and having a step width of 0.5 m (red curves in Figure 4). As counterpart, the average empirical detection rate and its confidence envelope (Equation (8)) was evaluated by comparison of the single-scan TLS detections with the reference data of the complete tree list. For comparison with the model-based estimates, the average empirical detection rates were likewise calculated using a sequence of sample plot radii ranging from 3 to 20 m but having a step width of 1 m (black line in Figure 4).
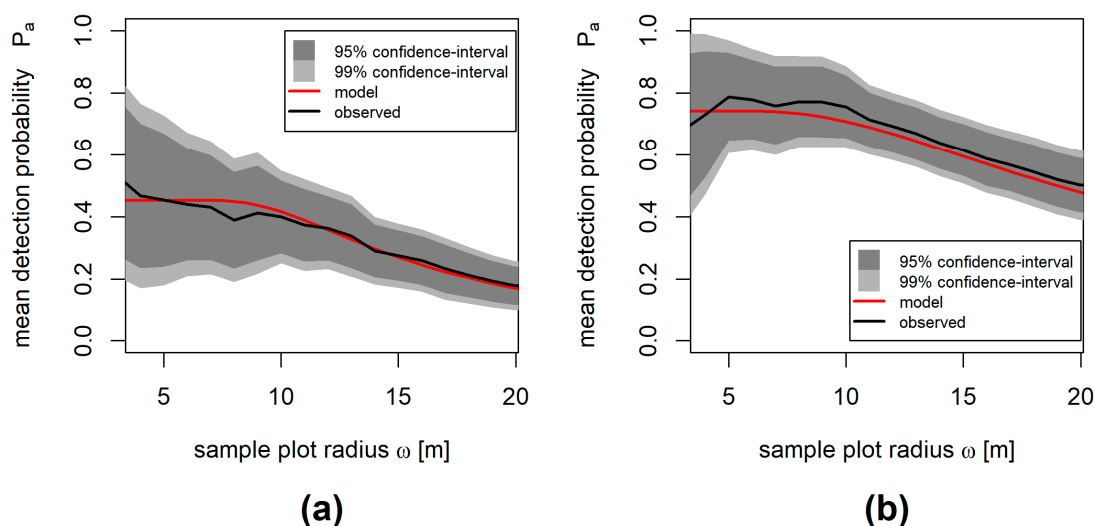
Figure 4. Mean detection probability P_a for different sample plot radii ω using TLS in single-scan mode for both strata. The black line represents the observed data; the red line represents the model prediction. The light and dark grey areas are the 99% and 95% confidence intervals computed from the observed data, respectively. (**a**) Small trees (5 cm ≤ dbh < 20 cm) and (**b**) large trees (dbh ≥ 20 cm).

The results showed for both tree size strata that the two curves had similar shapes: the curve of the model estimates and the curve of the average empirical detection rates. Hence, the model was able to describe the general trend of a decreasing detection rate with increasing sample plot radius ω. For the stratum of the smaller trees (5 cm ≤ dbh < 20 cm), the maximum absolute deviation between the modeled and the empirical average detection rate was 0.060, with a sample plot radius of $\omega = 8$ m

(Figure 4a). For the stratum of the larger trees (dbh ≥ 20 cm), the maximum absolute deviation was 0.048, with a $\omega = 10$ m radius (Figure 4b). In addition, the curves of the model estimates lay close to the center of the 95% envelopes of the empirical average detection rates.

3.1.3. Results of the Simulation Study

For both tree size strata and across the entire sequence of sample plot radii, the expectation of the model-based estimate was close to the expectation of the empirical detection rate (Figure 5a,b). For the smaller trees, the model had a slightly negative bias for sample plot radii of less than 5 m, and it had a positive bias for radii larger than 10 m (Figure 5c). The largest absolute bias of 0.0163 was produced with a radius of 13 m. For the larger trees, the model behaved nearly unbiased with sample plot radii smaller than 7 m (Figure 5d). However, with radii larger than 10 m, a positive bias likewise occurred. For the thicker trees, the largest absolute bias was 0.0162 with a sample plot radius of 14 m.
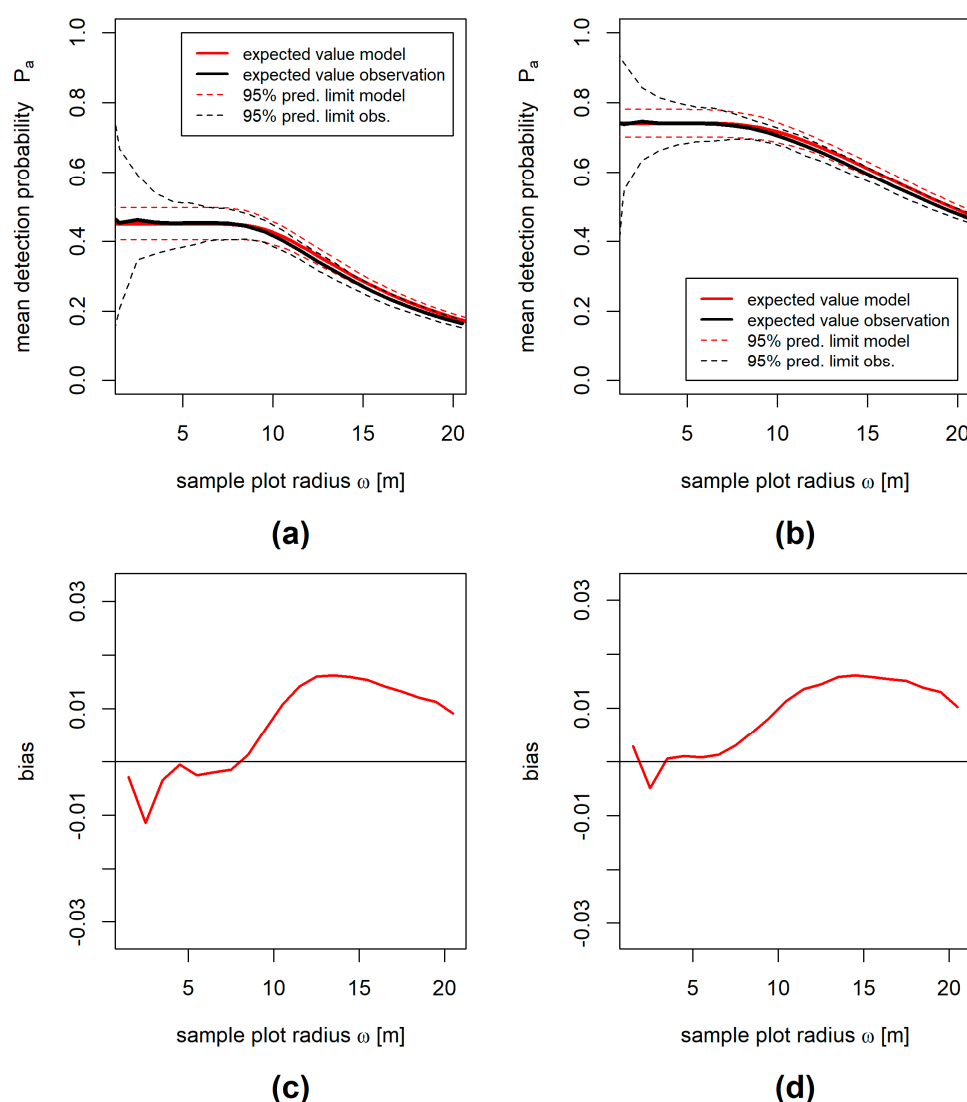
Figure 5. Results of the simulation study (200 simulation runs of 25 sample plots) for both strata, using annuli of 1 m widths for model fitting to the simulated single-scan data. (**a**,**b**) Mean detection probability P_a for different sample plot radii ω using simulated TLS in multi-scan mode. The solid black line represents the expectation of the simulated data; the solid red line represents the expectation of the model prediction. The dashed lines represent the corresponding 95% prediction limits, i.e., the 2.5% and 97.5% quantiles of the 200 simulation runs. (**c**,**d**) Model bias dependent on the sample plot radius. (**a**,**c**) Small trees (5 cm ≤ dbh < 20 cm) and (**b**,**d**) large trees (dbh ≥ 20 cm).

3.2. Modeling the Detection Probability of TLS in Multi-Scan Mode

In the following section, the results are presented in detail for the "scan variant 3" of the scanner position layouts described by Gollob et al. [43], i.e., a triangle-shaped alignment of scanner positions, including an additional central scan (Figure 6). This layout was the best compromise between necessary sampling effort and detection rate [43]. Further results of the nine different layouts from Gollob et al. [43] are outlined in the Appendix A (Figures A1 and A2 for the smaller tree size stratum, and Figures A3 and A4 for the larger tree size stratum).

(a)   **(b)**
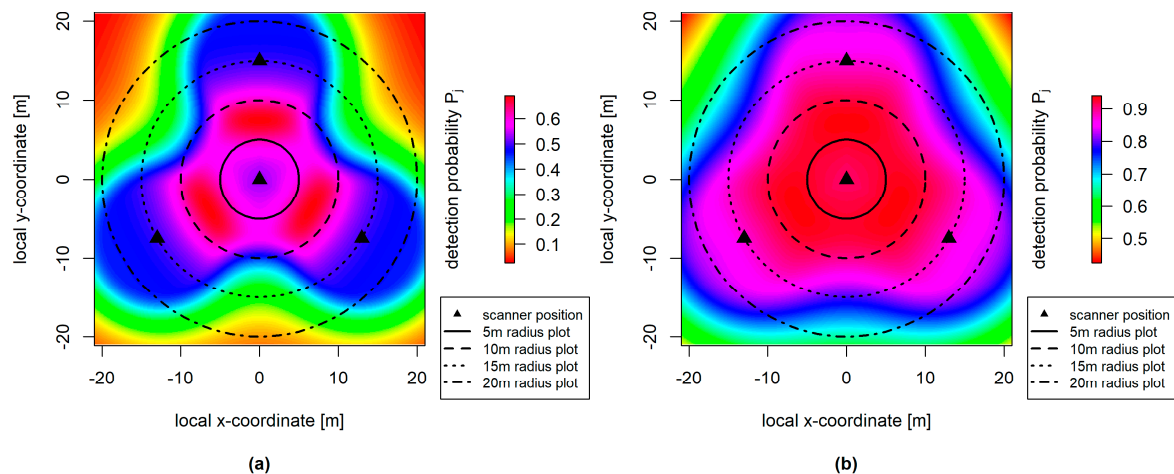
Figure 6. Distance-dependent detection probabilities P_j for multi-scan TLS for both strata. Cell size of the raster is 1 cm × 1 cm. (**a**) Small trees (5 cm ≤ dbh < 20 cm) and (**b**) large trees (dbh ≥ 20 cm).

When the joint detection probability under the three scanner positions was evaluated, it became obvious that the area with the highest detection probabilities was neither located at the sample plot center nor nearby the scanner positions. Trees were instead most likely detected in the interspace between the central positions and the outer positions of the scanner (Figure 6). More precisely, the area with the highest detection probability was located within the annulus having an inner radius of 5 m and an outer radius of 10 m.

For the model-based estimate of the detection rate, the local estimates of the joint detection probabilities on the fine grid were averaged within the sample plot area. The estimates of P_a for different sample plot radii ω, calculated as the arithmetic mean of all raster cells within a sample plot of the corresponding radius, are presented in Figure 7. For both strata, the model predictions fell within the 95% envelope of the average empirical detection rates. The maximum absolute deviation between the empirical detection rates and the model-based estimates was 0.095 with a sample plot radius of 5 m for the smaller trees, and it was 0.088 with a 20 m plot radius for the larger trees, respectively (Figure 7).

When the model-based estimates were compared with the empirical detection rates from the simulations, the bias was throughout positive across the entire range of plot radii and for both tree size strata (Figure 8). The average bias for the smaller trees was 0.0195, its minimum was 0.0120, and its maximum was 0.0242. The average bias for the larger trees was 0.0052, and its minimum and maximum were 0.0035 and 0.0064, respectively.
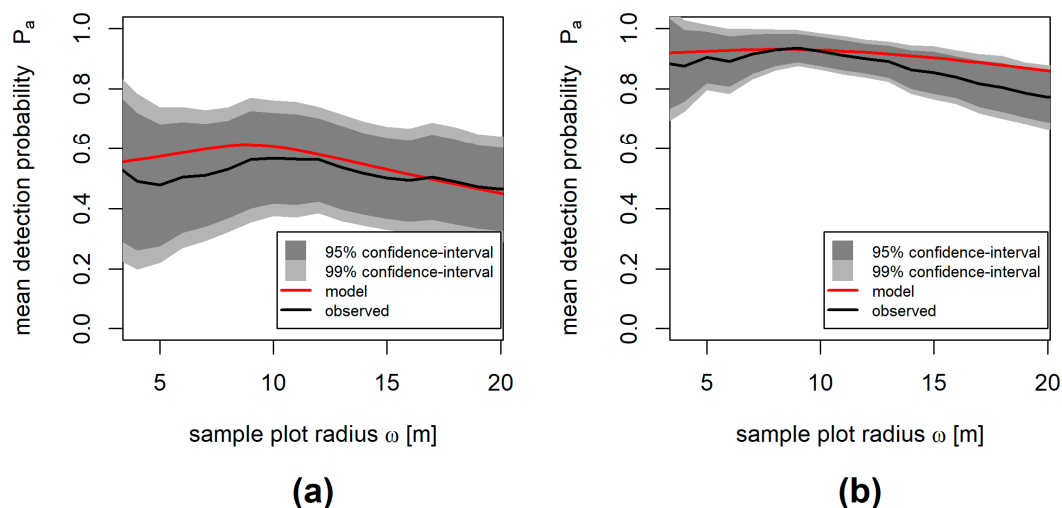
Figure 7. Mean detection probability P_a for different sample plot radii ω using TLS in multi-scan mode for both strata (small trees, left and large trees, right). The black line represents the observed data; the red line represents the model prediction. The light and dark grey areas are the 99% and 95% confidence intervals computed from the observed data, respectively. (**a**) Small trees (5 cm $\leq$ dbh < 20 cm) and (**b**) large trees (dbh $\geq$ 20 cm).

3.3. Discretization Bias

To examine whether the overestimation was simply produced by the binning of the distances into 1 m wide classes, an extra simulation was conducted using a smaller class width of only 0.1 m. When the distances were binned into such 0.1 m wide classes, the maximum absolute bias of the model-based estimator was 0.0026 for the smaller tree size stratum, and it was 0.0006 for the larger trees (Figure 9). Hence, the bias became negligibly small through this fine binning. As a consequence, the proposed estimator was considered as approximately unbiased, given such a fine class width was used for the binning of the measured center-to-tree distances.
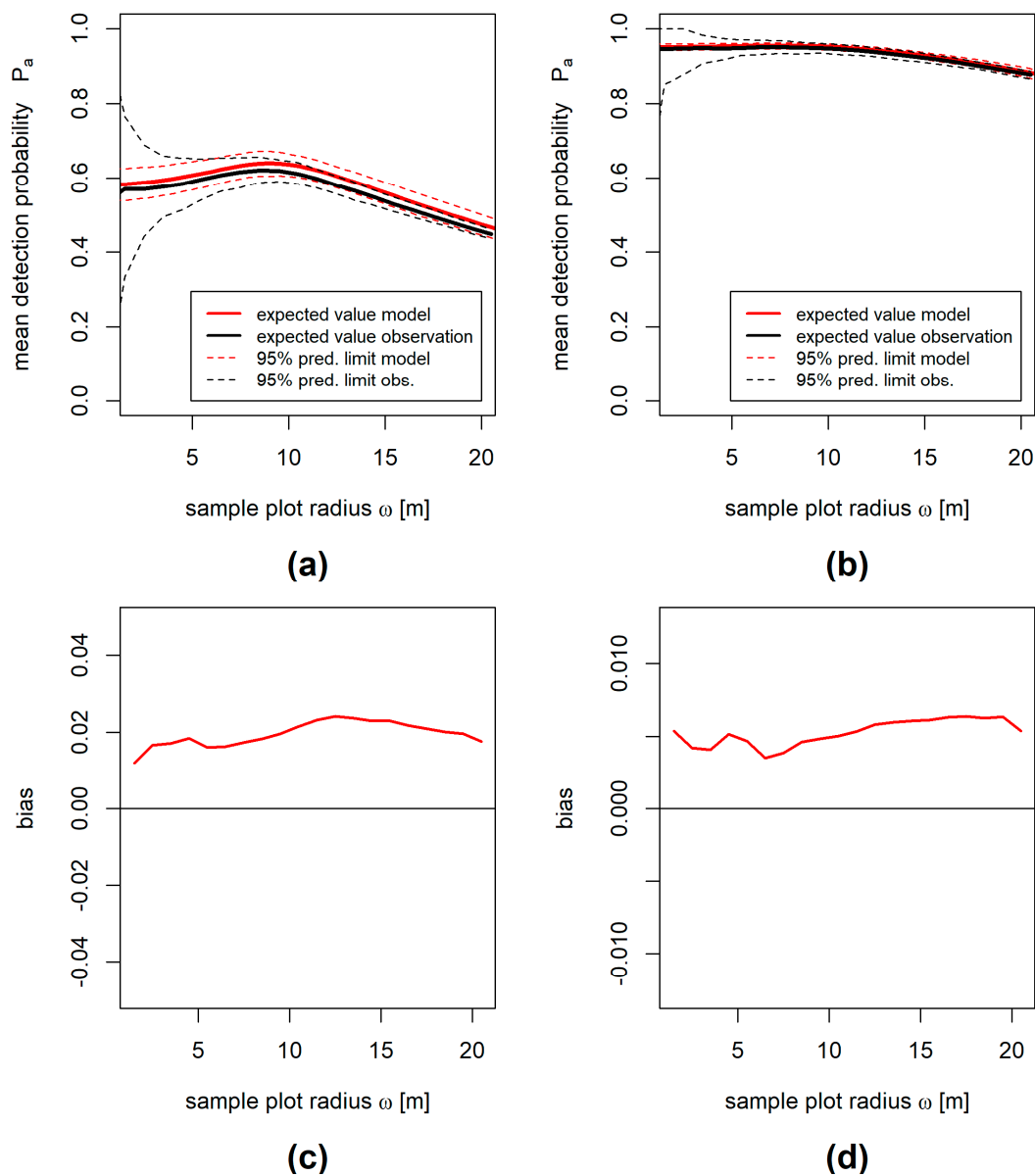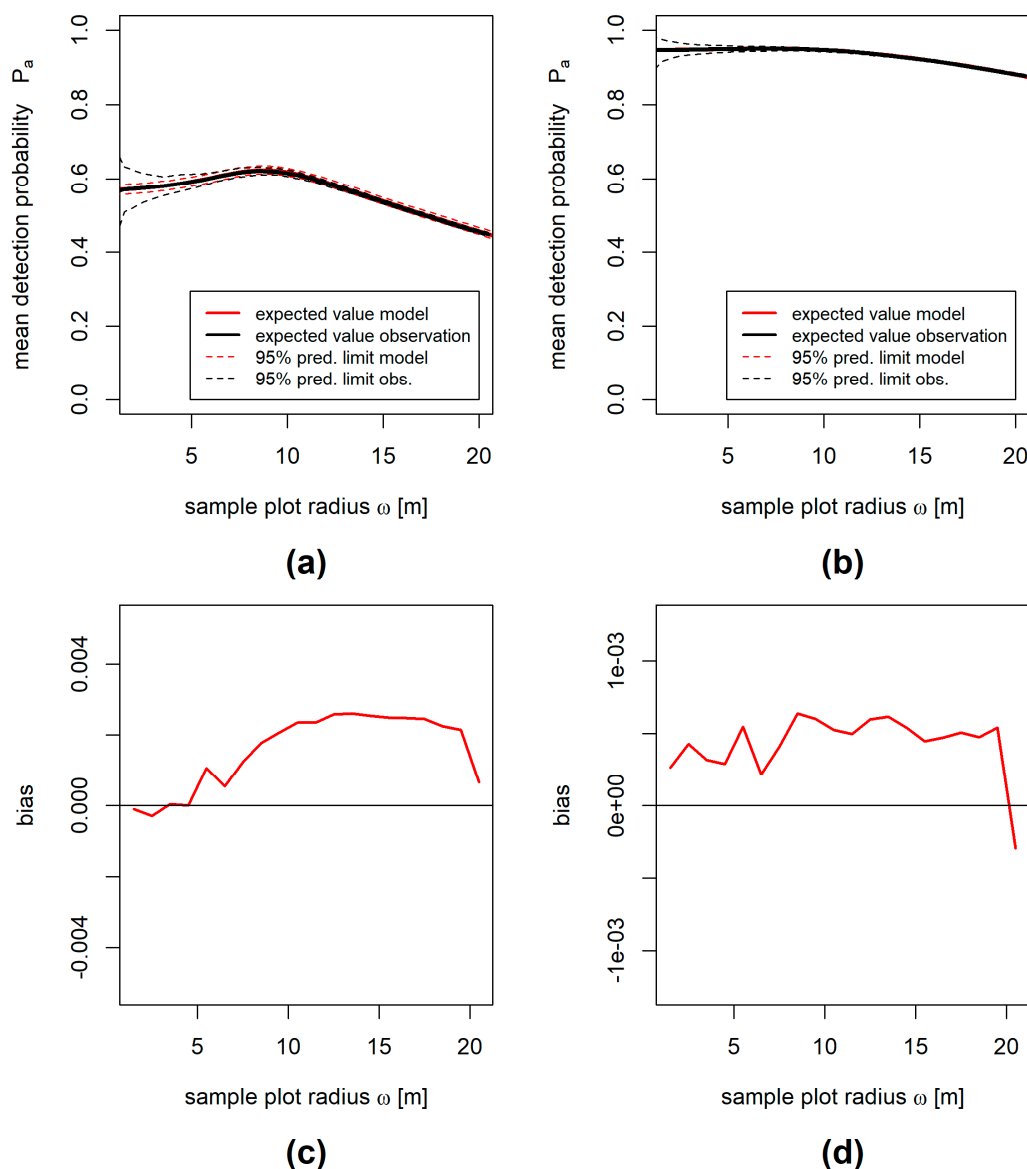
Figure 8. Results of the simulation study (200 simulation runs of 25 sample plots) for both strata, using annuli of 1 m widths for model fitting to the simulated multi-scan data. (**a**,**b**) Mean detection probability P_a for different sample plot radii ω using simulated TLS in multi-scan mode. The solid black line represents the expectation of the simulated data; the solid red line represents the expectation of the model prediction. The dashed lines represent the corresponding 95% prediction limits, i.e., the 2.5% and 97.5% quantiles of the 200 simulation runs. (**c**,**d**) Model bias dependent on the sample plot radius. (**a**,**c**) Small trees (5 cm ≤ dbh < 20 cm) and (**b**,**d**) large trees (dbh ≥ 20 cm).

Figure 9. Results of the simulation study (200 simulation runs of 250 sample plots) for both strata, using annuli of 0.1 m widths for model fitting to the simulated multi-scan data. (**a**,**b**) Mean detection probability P_a for different sample plot radii ω using simulated TLS in multi-scan mode. The solid black line represents the expectation of the simulated data; the solid red line represents the expectation of the model prediction. The dashed lines represent the corresponding 95% prediction limits, i.e., the 2.5% and 97.5% quantiles of the 200 simulation runs. (**c**,**d**) Model bias dependent on the sample plot radius. (**a**,**c**) Small trees (5 cm $\leq$ dbh $<$ 20 cm) and (**b**,**d**) large trees (dbh $\geq$ 20 cm).

4. Discussion

4.1. Vailidity of Model Assumptions

In the classic distance sampling approach [46–49], a strong assumption is made with a complete detection at $r = 0$. Such as demonstrated by Ducey and Astrup [21] and Astrup et al. [42], this assumption may hold as long as the tree locations were identified with semi-automatic approaches. However, it was demonstrated by our study that this assumption was actually not met if the tree detection was performed with fully automated routines. Consequently, any uncritical adoption of the classic distance sampling methods would have resulted in a severe overestimation of P_a (Table 2) and thus, in an underestimation of the actual stem density.

Regardless of the assumption outlined above, the novel presented model framework assumes that the detectability of a tree is isotropic, i.e., it only depends on the scanner-to-tree distance and not on the direction in which the scanner is relatively located to the tree. Therefore, the detectability of a tree becomes independent for all scanner positions.

In fact, these assumptions are simplifications of the real world. In reality, situations occur where a tree can easily be detected from one direction, whereas it is completely shaded from another direction. Moreover, trees can show particular characteristics, such as, e.g., a forked or a tilted stem, making the automatic tree detection challenging, regardless of the scanner-to-tree distance. These phenomena can lead to violations of the model assumptions and may cause an extra noise or may even introduce a model bias. However, the simulation studies showed that the new estimator is (approximately) unbiased in the case that the model assumptions hold and if the observation distances are binned into fine classes. With the available real-world data, the modeled P_a fell within the confidence envelopes of the estimates, and the observed trend (e.g., the peak of P_a between $r = 5$ m and $r = 10$ m for the multi-scan data) was properly reflected by the model. Thus, the novel model-based approach is particularly useful for the planning and optimization of multi-scan TLS sampling campaigns.

4.2. Discretization Bias

The observed detection probabilities were calculated for discrete annuli, finally resulting in a small positive model bias. A possible reason for this bias was that a constant detection probability was assumed for each annulus, only dependent on the distance between the scanner and the centerline of the annulus. However, by fitting the model to the unweighted average detection probabilities per distance class, it is not possible to consider that the slope of the detection function generally changes within the range of an annulus. Consequently, the model showed almost unbiased when the detection function was almost linear and significantly biased results in the case that the detection function was strongly curved.

As an intuitive solution of this problem, the width of the annuli can be reduced, as infinitesimally small annuli would result in an (approximately) unbiased model. In practical applications, such a reduction of the annuli width has limitations, as the number of trees within each annulus decreases with the decreasing annulus width. Especially with small sample sizes, the number of observations per distance classes becomes very small, and missing data is likely produced. Thus, the useable minimum width of the annuli depends on the sample size, and for relatively small sample sizes, a discretization bias is unavoidable with the presented model framework.

Logistic regression models would overcome the necessity of discretization; however, trials showed no satisfactory results, as the logistic curve lacks the shoulder of the hazard-rate function and, thus, does not fit the observed data well. The applicability of gamma, log-logistic, or Tweedie models to overcome these limitations of the classic logistic model will be a worthwhile focus for future research.

4.3. Necessary a Priori Data and Transferability of the Results

Key of the classic distance sampling approach [46–49] is that only distances between the observer (laser scanner) and the detected objects (trees) are measured to achieve inference on the detection probability. That is, single-scan TLS data is sufficient for the modeling of *g(r)* and likewise for the estimation of P_j. In cases when the assumption of classic distance sampling hold, i.e., perfect detectability at $r = 0$ is given, the labor effort to obtain the required measurement data is only small.

Contrary to this, in the case of an imperfect detection at $r = 0$, the modified approach to estimate *g(r)* requires extra measurement data in terms of manually collected reference data. In fact, the collection of complete ground truth data is impractical and seems contradictory to the general demand for fully automated routines with TLS data. However, the advantages of an optimized layout definitely justify the conduction of a prior study to collect the required reference data at least on a subsample of plots.

Parameters of the estimated detection function depend on (i) the resolution and range of the scanning equipment, (ii) the visibility in the area of interest, and (iii) the algorithms used for tree detection

from the point clouds. Regarding the remarkable differences between the detection probabilities obtained with different algorithms [8], we cannot recommend to use parameter estimates obtained from different tree detection algorithms. However, when older single-scan TLS and reference data were available that were obtained with similar scanning equipment in the same area of interest or in an area with similar sighting conditions, it was possible to reuse this prior information for the model fitting.

4.4. Model Interpretation and Possibilities for Further Model Applications

Our model framework enables the prediction of detection rates for the different sample plot sizes and helps to explain trends that were observed in the real-world data. When P_a was estimated under the multi-scan layout, it became obvious that the area with the highest detection probabilities was neither located at the sample plot center nor nearby the scanner positions. Trees were instead most likely detected in the interspace between the central positions and the outer positions of the scanner (Figure 6). This finding explained why Gollob et al. [43] reported the general trend of decreasing detection probability with increasing sample plot radius but observed a trend reversal for small sample plots (<10 m). More precisely, the area with the highest detection probability was located within the annulus, having an inner radius of 5 m and an outer radius of 10 m. Hence, the mean detection probability P_a on a 10 m radius plot became higher than on the 5 m radius plot.

The presented model framework can be easily adopted to estimate the detection probabilities also under other sample plot shapes (e.g., rectangles or polygons) and different scanner position layouts. In future research projects, we will further examine the effects of different spacing between the scanner positions. Moreover, the model framework is also useful for post-hoc corrections of the nondetection bias with multi-scan TLS-based forest inventories. However, as the correction method is globally applied, an adjustment of the plot-level estimates is simply not feasible. As an additional drawback, a variance estimator of the correction method is still lacking. Hence, in future studies, we will test simulation-based estimators, and we will examine their influence on the overall precision of the TLS-based estimates.

5. Conclusions

Since the labor effort of multi-scan TLS is higher than with traditional measurement instruments, a further improvement or optimization of the sampling scheme is necessary. The methodology presented in this study allows a model-based comparison of the detection probabilities with different scanning position layouts, sample plot sizes, and shapes for multi-scan TLS applications in the forest inventory context. The extra effort to obtain the a priori reference data required for the model fitting is justified by the benefits from a well-planned multi-scan layout, especially in larger sampling campaigns. Thus, our study is a step towards the optimization of multi-scan TLS applications and provides a helpful tool for the planning of multi-scan TLS-based forest inventories in the future.

Pending the development of a suitable variance estimator in the future, the methodology presented in this study might further be used to correct global estimates of the tree count for nondetection bias.

Some lessons for the practical applicability of TLS in the forest inventory context can be learned from this study. The possible shape of the sample plot should not be limited to a circle; arranging the scanner positions on a line and sampling a strip-shaped plot seems to be an interesting approach (scan variant 7 in Figures A1 and A2 in the Appendix A). The spacing of the scanner positions should be oriented at the width of the shoulder of the detection function (Figure 2), a spacing of more than approx. twice the width of the shoulder yields areas, with low detection probability in between the scanner positions (compare scan variants 7 and 8 in Figures A1 and A2 in the Appendix A). In case the target population only consists of larger trees, the spacing of the scanner positions can therefore be increased without a loss of detectability, enabling the sampling of larger areas with a constant number of scans. In case a circular sample plot is scanned, one scan position should be located at the plot center (compare scan variants 1 vs. 2, 3 vs. 4, 5 vs. 6, and 7 vs. 8 in Figures A1 and A2 in the Appendix A).

Appendix A

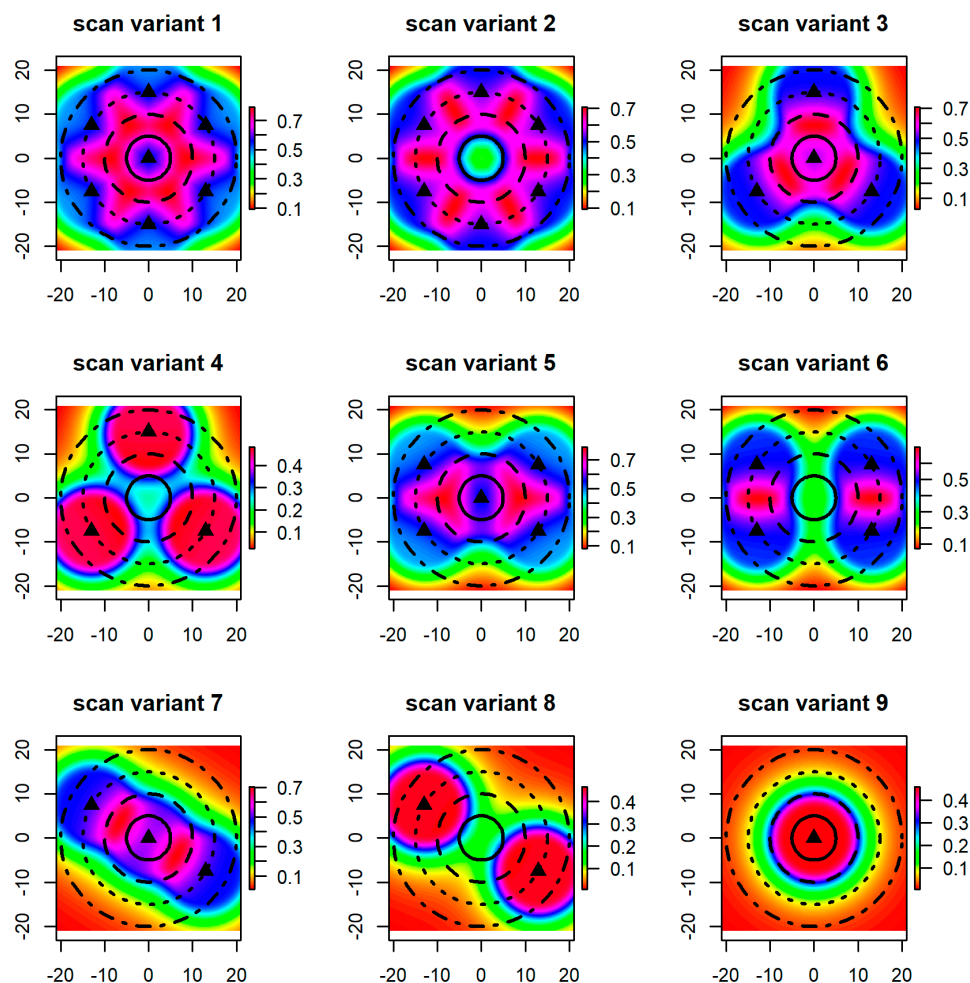**Figure A1.** Distance-dependent detection probabilities $P(d_j)$ of small trees (5 cm ≤ dbh < 20 cm) for all scan variants described by Gollob et al. [43]. Black triangles indicate the scanner positions; the different dashed lines indicate circular sample plots with 5, 10, 15, and 20 m radii, respectively. Axis labels are the local x- and y-coordinates (m). Cell size of the raster is 1 cm × 1 cm.

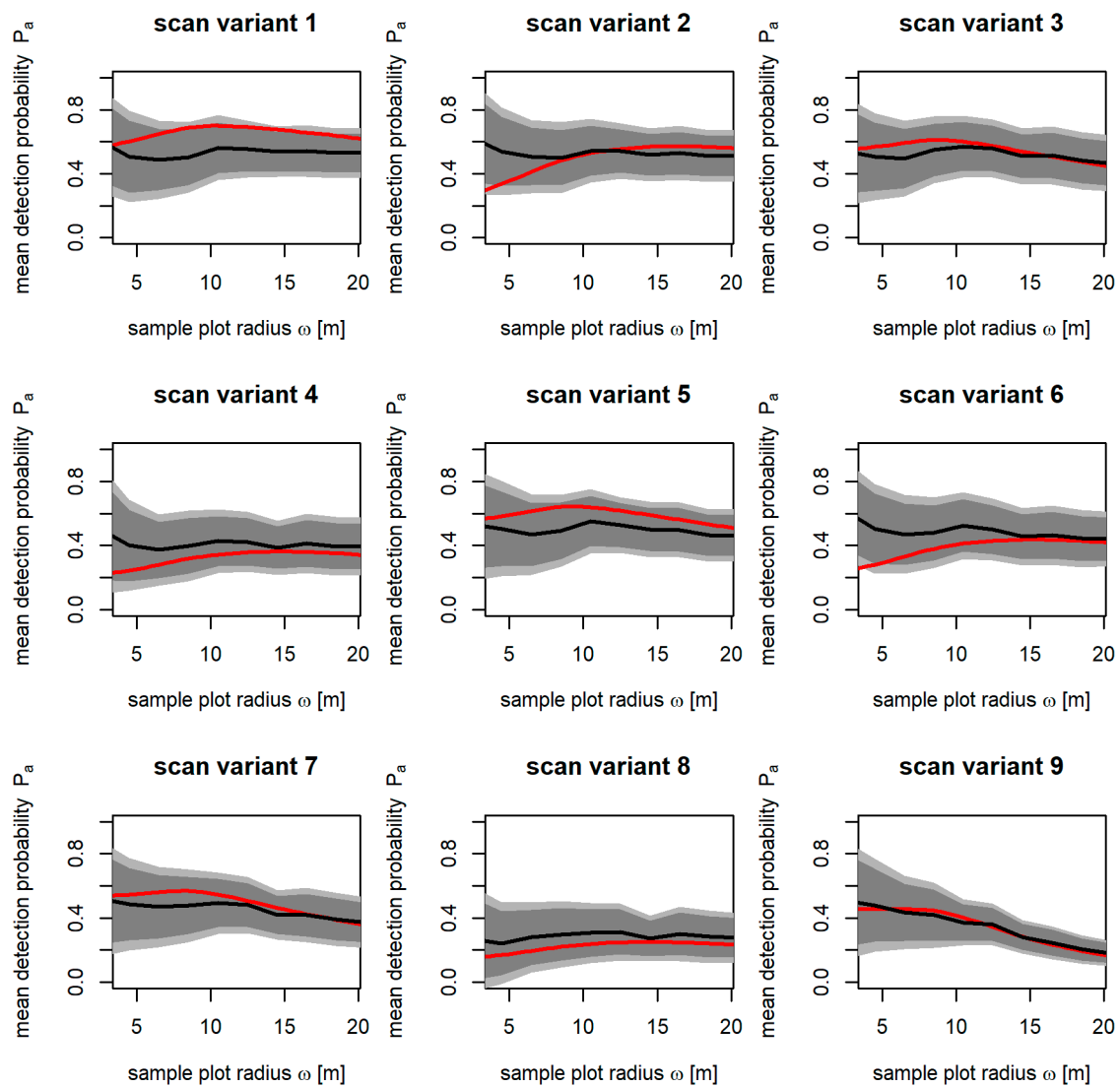**Figure A2.** Mean detection probability P_a of small trees (5 cm ≤ dbh < 20 cm) for different sample plot radii ω and all scan variants described by Gollob et al. [43]. The black line represents the observed data; the red line represents the model prediction. The light and dark grey areas are the 99% and 95% confidence intervals computed from the observed data, respectively.
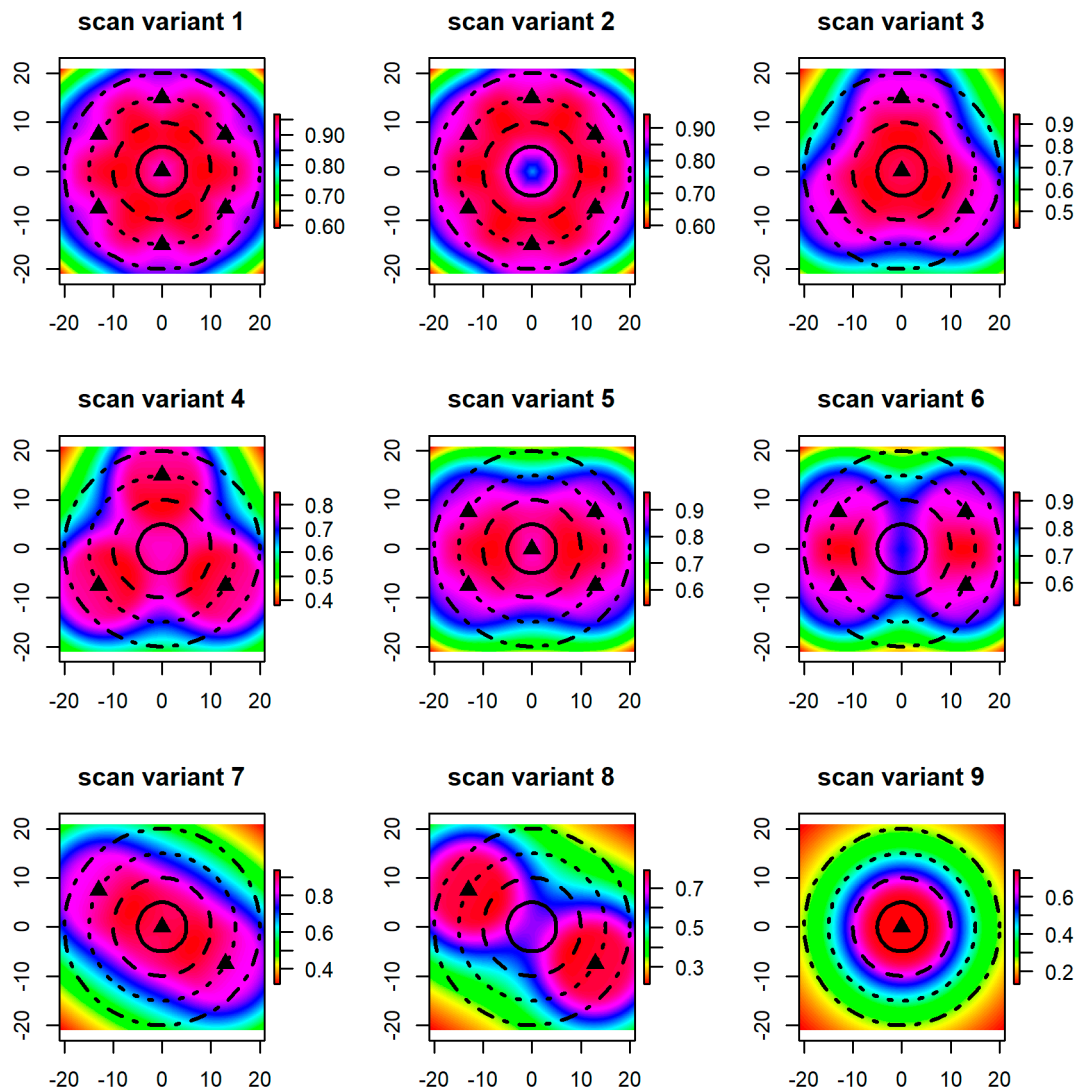
Figure A3. Distance-dependent detection probabilities $P(d_j)$ of large trees (dbh $\geq$ 20 cm) for all scan variants described by Gollob et al. [43]. Black triangles indicate the scanner positions; the different dashed lines indicate circular sample plots with 5, 10, 15, and 20 m radii, respectively. Cell size of the raster is 1 cm $\times$ 1 cm.
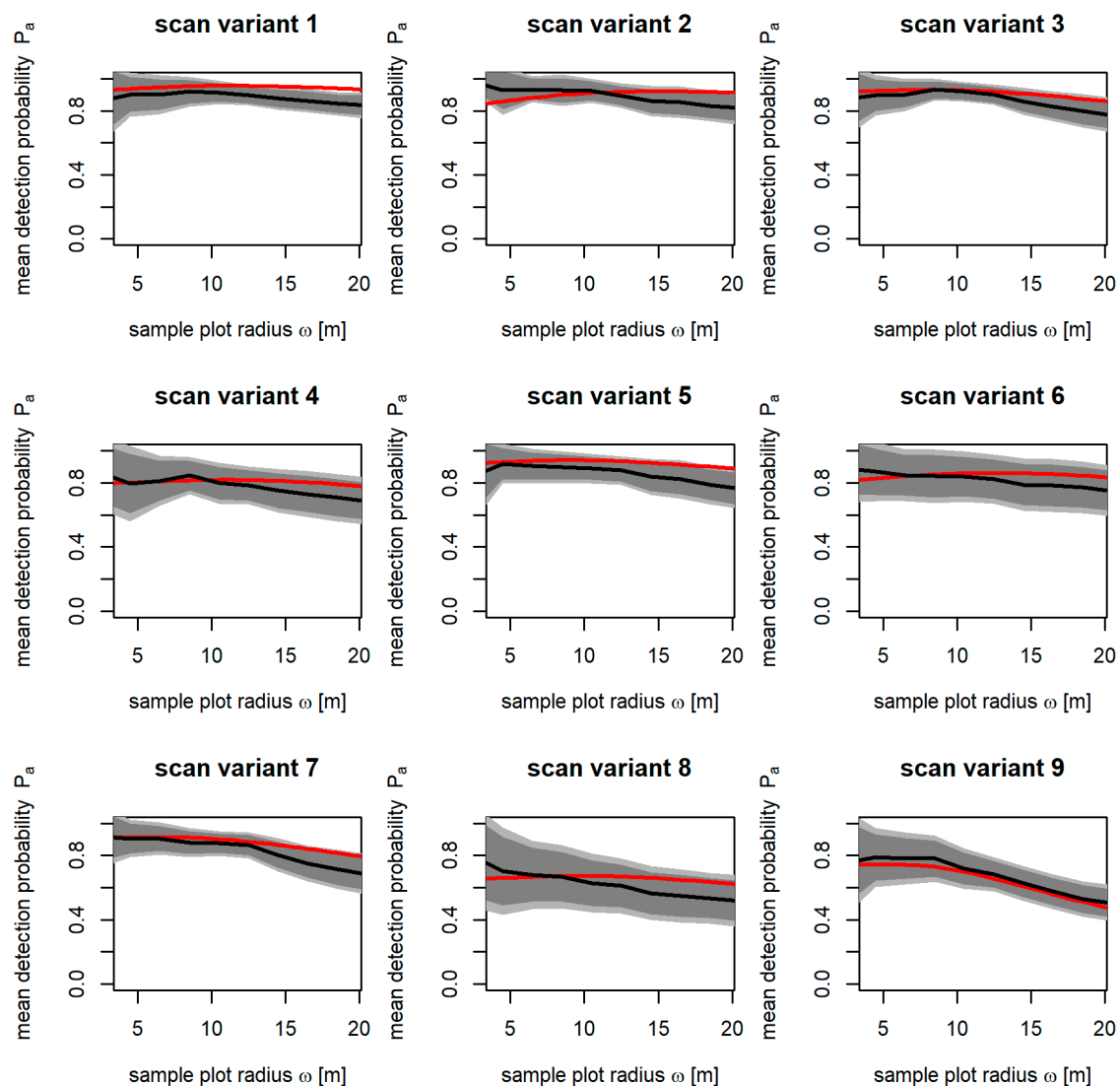
Figure A4. Mean detection probability P_a of large trees (dbh ≥ 20 cm) for different sample plot radii ω and all scan variants described by Gollob et al. [43]. The black line represents the observed data; the red line represents the model prediction. The light and dark grey areas are the 99% and 95% confidence intervals computed from the observed data, respectively.

References

1. Köhl, M.; Magnussen, S.; Marchetti, M. *Sampling Methods, Remote Sensing and GIS Multiresource Forest Inventory*; Tropical Forestry; Springer: Berlin/Heidelberg, Germany, 2006; ISBN 978-3-540-32571-0.
2. Ministerial Conference on the Protection of Forests in Europe (MCPFE) Liaison Unit. *State of Europe's Forests 2003*; The MCPFE Report on Sustainable Forest Management in Europe; Ministerial Conference on the Protection of Forests in Europe (MCPFE) Liaison Unit: Vienna, Austria, 2003.
3. IUFRO Research Group. *Guidelines for Designing Multipurpose Resource Inventories*; A Project of IUFRO Research Group 4.02.02; Lund, H.G., Ed.; IUFRO Research Group: Vienna, Austria, 1998; Volume 8.
4. Kenning, R.S.; Ducey, M.J.; Brissette, J.C.; Gove, J.H. Field efficiency and bias of snag inventory methods. *Can. J. For. Res.* **2005**, *35*, 2900–2910. [CrossRef]
5. Kershaw, J.A.; Ducey, M.J.; Beers, T.W.; Husch, B. *Forest Mensuration*; John Wiley & Sons, Ltd.: Chichester, UK, 2016; ISBN 9781118902028.
6. Kauffman, J.B.; Arifanti, V.B.; Basuki, I.; Kurnianto, S.; Novita, N.; Murdiyarso, D.; Donato, D.C.; Warren, M.W. *Protocols for the Measurement, Monitoring, and Reporting of Structure, Biomass, Carbon Stocks and Greenhouse Gas Emissions in Tropical Peat Swamp Forests*; Center for International Forestry Research: Bogor, Indonesia, 2017.

7. Liang, X.; Kankare, V.; Hyyppä, J.; Wang, Y.; Kukko, A.; Haggrén, H.; Yu, X.; Kaartinen, H.; Jaakkola, A.; Guan, F.; et al. Terrestrial laser scanning in forest inventories. *ISPRS J. Photogramm. Remote Sens.* **2016**, *115*, 63–77. [CrossRef]

8. Liang, X.; Hyyppä, J.; Kaartinen, H.; Lehtomäki, M.; Pyörälä, J.; Pfeifer, N.; Holopainen, M.; Brolly, G.; Francesco, P.; Hackenberg, J.; et al. International benchmarking of terrestrial laser scanning approaches for forest inventories. *ISPRS J. Photogramm. Remote Sens.* **2018**, *144*, 137–179. [CrossRef]

9. Ritter, T.; Schwarz, M.; Tockner, A.; Leisch, F.; Nothdurft, A. Automatic Mapping of Forest Stands Based on Three-Dimensional Point Clouds Derived from Terrestrial Laser-Scanning. *Forests* **2017**, *8*, 265. [CrossRef]

10. Mandallaz, D. *Sampling Techniques for Forest Inventories*; Chapman and Hall/CRC: Boca Raton, FL, USA, 2008.

11. Gregoire, T.G.; Valentine, H.T. *Sampling Strategies for Natural Resources and Environment*; Chapman and Hall/CRC: Boca Raton, FL, USA, 2008.

12. Seidel, D.; Ammer, C. Efficient measurements of basal area in short rotation forests based on terrestrial laser scanning under special consideration of shadowing. *IForest Biogeosci. For.* **2014**, 226–231. [CrossRef]

13. Litkey, P.; Liang, X.; Kaartinen, H.; Hyyppä, J.; Kukko, A.; Holopainen, M. Single-scan TLS methods for forest parameter retrieval. In Proceedings of the SilviLaser 8th International Conference on LiDAR Applications in Forest Assessment and Inventory, La Grande Motte, France, 17–19 September 2008; Heriot-Watt University: Edinburgh, UK; pp. 295–304.

14. Reddy, R.S.; Jha, C.S.; Rajan, K.S. Automatic Tree Identification and Diameter Estimation Using Single Scan Terrestrial Laser Scanner Data in Central Indian Forests. *J. Indian Soc. Remote Sens.* **2018**, *46*, 937–943. [CrossRef]

15. Oveland, I.; Hauglin, M.; Giannetti, F.; Kjørsvik, N.S.; Gobakken, T. Comparing three different ground based laser scanning methods for tree stem detection. *Remote Sens.* **2018**, *10*, 538. [CrossRef]

16. Hauglin, M.; Gobakken, T.; Astrup, R.; Ene, L.; Næsset, E. Estimating single-tree crown biomass of norway spruce by airborne laser scanning: A comparison of methods with and without the use of terrestrial laser scanning to obtain the ground reference data. *Forests* **2014**, *5*, 384–403. [CrossRef]

17. Lovell, J.L.; Jupp, D.L.B.; Newnham, G.J.; Culvenor, D.S. Measuring tree stem diameters using intensity profiles from ground-based scanning lidar from a fixed viewpoint. *ISPRS J. Photogramm. Remote Sens.* **2011**, *66*, 46–55. [CrossRef]

18. Murphy, G.E.; Acuna, M.A.; Dumbrell, I. Tree value and log product yield determination in radiata pine (*Pinus radiata*) plantations in Australia: Comparisons of terrestrial laser scanning with a forest inventory system and manual measurements. *Can. J. For. Res.* **2010**, *40*, 2223–2233. [CrossRef]

19. Brolly, G.; Király, G. Algorithms for Stem Mapping by Means of Terrestrial Laser Scanning. *Acta Silv. Lignaria Hung.* **2009**, *5*, 119–130.

20. Liang, X.; Litkey, P.; Hyyppa, J.; Kaartinen, H.; Vastaranta, M.; Holopainen, M. Automatic Stem Mapping Using Single-Scan Terrestrial Laser Scanning. *IEEE Trans. Geosci. Remote Sens.* **2012**, *50*, 661–670. [CrossRef]

21. Ducey, M.J.; Astrup, R. Adjusting for nondetection in forest inventories derived from terrestrial laser scanning. *Can. J. Remote Sens.* **2013**, *39*, 410–425.

22. Simonse, M.; Aschoff, T.; Spiecker, H.; Thies, M. *Automatic Determination of forest Inventory Parameters Using Terrestrial Laser Scanning*; ScandLaser Scientific Workshop on Airborne Laser Scanning of Forests; Albert Ludwigs University: Freiburg, Germany, 2003; Volume 2003, pp. 252–258.

23. Eysn, L.; Pfeifer, N.; Ressl, C.; Hollaus, M.; Grafl, A.; Morsdorf, F.; Ressl, C.; Eysn, L.; Pfeifer, N.; Morsdorf, F.; et al. A Practical Approach for Extracting Tree Models in Forest Environments Based on Equirectangular Projections of Terrestrial Laser Scans. *Remote Sens.* **2013**, *5*, 5424–5448. [CrossRef]

24. Yao, T.; Yang, X.; Zhao, F.; Wang, Z.; Zhang, Q.; Jupp, D.; Lovell, J.; Culvenor, D.; Newnham, G.; Ni-Meister, W.; et al. Measuring forest structure and biomass in New England forest stands using Echidna ground-based lidar. *Remote Sens. Environ.* **2011**, *115*, 2965–2974. [CrossRef]

25. Calders, K.; Newnham, G.; Burt, A.; Murphy, S.; Raumonen, P.; Herold, M.; Culvenor, D.; Avitabile, V.; Disney, M.; Armston, J.; et al. Nondestructive estimates of above-ground biomass using terrestrial laser scanning. *Methods Ecol. Evol.* **2015**, *6*, 198–208. [CrossRef]

26. Heinzel, J.; Huber, M.O. Constrained spectral clustering of individual trees in dense forest using terrestrial laser scanning data. *Remote Sens.* **2018**, *10*, 1056. [CrossRef]

27. Liu, C.; Xing, Y.; Duanmu, J.; Tian, X. Evaluating different methods for estimating diameter at breast height from terrestrial laser scanning. *Remote Sens.* **2018**, *10*, 513. [CrossRef]

28. Thies, M.; Pfeifer, N.; Winterhalder, D.; Gorte, B.G.H. Three-dimensional reconstruction of stems for assessment of taper, sweep and lean based on laser scanning of standing trees. *Proc. Scand. J. For. Res.* **2004**, *19*, 571–581. [CrossRef]
29. Maas, H.-G.; Bienert, A.; Scheller, S.; Keane, E. Automatic forest inventory parameter determination from terrestrial laser scanner data. *Int. J. Remote Sens.* **2008**, *29*, 1593–1879. [CrossRef]
30. Ritter, T.; Nothdurft, A. Automatic assessment of crown projection area on single trees and stand-level, based on three-dimensional point clouds derived from terrestrial laser-scanning. *Forests* **2018**, *9*, 237. [CrossRef]
31. Watt, P.J.; Donoghue, D.N.M. Measuring forest structure with terrestrial laser scanning. *Int. J. Remote Sens.* **2005**, *26*, 1437–1446. [CrossRef]
32. Liang, X.; Hyyppä, J. Automatic Stem Mapping by Merging Several Terrestrial Laser Scans at the Feature and Decision Levels. *Sensors* **2013**, *13*, 1614–1634. [CrossRef] [PubMed]
33. Liang, X.; Kankare, V.; Yu, X.; Hyyppa, J.; Holopainen, M. Automated Stem Curve Measurement Using Terrestrial Laser Scanning. *IEEE Trans. Geosci. Remote Sens.* **2014**, *52*, 1739–1748. [CrossRef]
34. Hilker, T.; Coops, N.C.; Culvenor, D.S.; Newnham, G.; Wulder, M.A.; Bater, C.W.; Siggins, A. A simple technique for co-registration of terrestrial LiDAR observations for forestry applications. *Remote Sens. Lett.* **2012**, *3*, 239–247. [CrossRef]
35. Antonarakis, A.S. Evaluating forest biometrics obtained from ground lidar in complex riparian forests. *Remote Sens. Lett.* **2011**, *2*, 61–70. [CrossRef]
36. Abegg, M.; Kükenbrink, D.; Zell, J.; Schaepman, M.; Morsdorf, F.; Abegg, M.; Kükenbrink, D.; Zell, J.; Schaepman, M.E.; Morsdorf, F. Terrestrial Laser Scanning for Forest Inventories—Tree Diameter Distribution and Scanner Location Impact on Occlusion. *Forests* **2017**, *8*, 184. [CrossRef]
37. Côté, J.-F.; Fournier, R.A.; Frazer, G.W.; Olaf Niemann, K. A fine-scale architectural model of trees to enhance LiDAR-derived measurements of forest canopy structure. *Agric. For. Meteorol.* **2012**, *166*, 72–85. [CrossRef]
38. Van der Zande, D.; Jonckheere, I.; Stuckens, J.; Verstraeten, W.W.; Coppin, P. Sampling design of ground-based lidar measurements of forest canopy structure and its effect on shadowing. *Can. J. Remote Sens.* **2008**, *34*, 526–538. [CrossRef]
39. Fardusi, M.J.; Fardusi, M.J.; Chianucci, F.; Barbati, A. Concept to Practice of Geospatial-Information Tools to Assist Forest Management and Planning under Precision Forestry Framework: A review. *Ann. Silvic. Res.* **2017**, *41*, 3–14. [CrossRef]
40. Olofsson, K.; Olsson, H. Estimating tree stem density and diameter distribution in single-scan terrestrial laser measurements of field plots: A simulation study. *Scand. J. For. Res.* **2018**, *33*, 365–377. [CrossRef]
41. Kuronen, M.; Henttonen, H.M.; Myllymäki, M. Correcting for nondetection in estimating forest characteristics from single-scan terrestrial laser measurements. *Can. J. For. Res.* **2019**, *49*, 96–103. [CrossRef]
42. Astrup, R.; Ducey, M.J.; Granhus, A.; Ritter, T.; von Lüpke, N. Approaches for estimating stand-level volume using terrestrial laser scanning in a single-scan mode. *Can. J. For. Res.* **2014**, *44*, 666–676. [CrossRef]
43. Gollob, C.; Ritter, T.; Wassermann, C.; Nothdurft, A. Influence of Scanner Position and Plot Size on the Accuracy of Tree Detection and Diameter Estimation Using Terrestrial Laser Scanning on Forest Inventory Plots. *Remote Sens.* **2019**, *11*, 1602. [CrossRef]
44. Liang, X.; Hyyppa, J.; Kukko, A.; Kaartinen, H.; Jaakkola, A.; Yu, A. The Use of a Mobile Laser Scanning System for Mapping Large Forest Plots. *IEEE Geosci. Remote Sens. Lett.* **2014**, *11*, 1504–1508. [CrossRef]
45. Trochta, J.; Král, K.; Janík, D.; Adam, D. Arrangement of terrestrial laser scanner positions for area-wide stem mapping of natural forests. *Can. J. For. Res.* **2013**, *43*, 355–363. [CrossRef]
46. Thomas, L.; Buckland, S.T.; Burnham, K.P.; Anderson, D.R.; Laake, J.L.; Borchers, D.L.; Strindberg, S. Distance Sampling. In *Encyclopedia of Environmetrics*; El-Shaarawi, A.H., Piegorsch, W.W., Eds.; John Wiley and Sons: Hoboken, NJ, USA, 2012; Volume 1, pp. 687–697.
47. Buckland, S.T.; Anderson, D.R.; Burnham, K.P.; Laake, J.L.; Borchers, D.L.; Thomas, L. *Introduction to Distance Sampling: Estimating Abundance of Biological Populations*; Oxford University Press: Oxford, UK, 2001.
48. Buckland, S.T.; Anderson, D.R.; Burnham, K.P.; Laake, J.L.; Borchers, D.L.; Thomas, L. *Advanced Distance Sampling: Estimating Abundance of Biological Populations*; Oxford University Press: Oxford, UK, 2004.
49. Anderson, D.R.; Pospahala, R.S. Correction of bias in belt transect sampling of immotile objects. *J. Wildl. Manag.* **1970**, *34*, 141–146. [CrossRef]
50. FARO FARO Laser Scanner Software—SCENE 6.2. Available online: https://faro.box.com/s/ipg53v1oio9qv1w5nlqfk6oyesyepix5 (accessed on 28 February 2020).

51. Isenburg, M. LAStools—Efficient LiDAR Processing Software (Version 160429, Academic). Available online: https://rapidlasso.com/lastools/ (accessed on 28 February 2017).

52. Rodriguez, A.; Laio, A. Clustering by fast search and find of density peaks. *Science* **2014**, *344*, 1492–1496. [CrossRef]

53. R Core Team. *A Language and Environment for Statistical Computing, R Version 3.5.1*; R Foundation for Statistical Computing: Vienna, Austria, 2020.

54. Quang, P.X. Nonparametric Estimators for Variable Circular Plot Surveys. *Biometrics* **1993**, *49*, 837–852. [CrossRef]

55. Akaike, H. Information theory and an extension of the maximum likelihood principle. In Proceedings of the 2nd International Symposium on Information Theory (USSR), Tsahkadsor, Armenia, 2–8 September 1971; Petrov, B.N., Csáki, F., Eds.; Akadémiai Kiadó: Budapest, Hungary, 1971; pp. 267–281.

56. Miller, D.L.; Rexstad, E.; Thomas, L.; Marshall, L.; Laake, J.L. Distance Sampling in R. *J. Stat. Softw.* **2019**, *89*. [CrossRef]

57. Dennis, J.; Gay, D.; Welsch, R. Algorithm 573: An Adaptive Nonlinear Least-Squares Algorithm. *ACM Trans. Math. Softw.* **1981**, *7*, 367–383. [CrossRef]